

Direct imaging of topological edges states with cold atoms

N. Goldman,¹ J. Dalibard,^{2,3} A. Dauphin,^{1,4} F. Gerbier,² M. Lewenstein,^{5,6} P. Zoller,^{7,8} and I. B. Spielman⁹

¹Center for Nonlinear Phenomena and Complex Systems - Université Libre de Bruxelles (U.L.B.), B-1050 Brussels, Belgium

²Laboratoire Kastler Brossel, CNRS, ENS, UPMC, 24 rue Lhomond, 75005 Paris

³Collège de France, 11, place Marcellin Berthelot, 75005 Paris, France

⁴Departamento de Física Teórica I, Universidad Complutense, 28040 Madrid, Spain

⁵ICFO – Institut de Ciències Fotòniques, Parc Mediterrani de la Tecnologia, 08860 Barcelona, Spain

⁶ICREA – Institució Catalana de Recerca i Estudis Avançats, 08010 Barcelona, Spain

⁷Institute for Quantum Optics and Quantum Information of the Austrian Academy of Sciences, A-6020 Innsbruck, Austria

⁸Institute for Theoretical Physics, Innsbruck University, A-6020 Innsbruck, Austria

⁹Joint Quantum Institute, National Institute of Standards and Technology,
and University of Maryland, Gaithersburg, Maryland, 20899, USA

(Dated: April 4, 2022)

Detecting topological order in cold-atom experiments is an outstanding challenge, the resolution of which offers novel perspectives on topological matter. In material systems, unambiguous signatures of topological order exist for topological insulators and quantum Hall devices. In quantum Hall systems, the quantized conductivity and the associated robust propagating edge modes – guaranteed by the existence of non-trivial topological invariants – have been observed through transport and spectroscopy measurements. Here, we show that optical-lattice-based experiments can be tailored to directly visualize the propagation of topological edge modes. Our method is rooted in the unique capability for initially *shaping* the atomic gas, and imaging its time-evolution after suddenly removing the shaping potentials. Our scheme, applicable to an assortment of atomic topological phases, provides the first method for imaging the dynamics of topological edge modes, directly revealing their angular velocity and spin structure.

The integer quantum Hall (QH) effect revolutionized our understanding of quantum matter, revealing the existence of exotic phases not described by the standard theory of phase transitions [1]. In this phenomenon, the Hall conductivity is quantized, $\sigma_H h/e^2 = \nu \in \mathbb{Z}$ (where e is the electron charge and h is Planck’s constant), whenever the Fermi energy resides in an energy gap. The integers ν are related to topological invariants – Chern numbers – that are associated with the bulk energy bands [1, 2]. Their topological origin guarantees that the Chern numbers are constant as long as the bulk gaps remain open, explaining the signature plateaus in the Hall resistivity, present when external parameters, such as magnetic fields, are varied. Moreover, a holographic principle stipulates that a topologically-ordered *bulk* gap, with topological invariant ν , necessarily hosts ν propagating modes localized on the samples *edge* [3]. These topological edge states are chiral – their motion has a well-defined orientation – inhibiting scattering processes in the presence of disorder.

In condensed matter physics, direct observations of edge states remain relatively rare. A first signature was obtained from magnetoplasmons created by pulsed voltages [4]. Another evidence arises from edge transport in engineered Aharonov-Bohm interferometers with QH systems [5]. By contrast the “routinely used” spectroscopic reconstruction of mid-gap states [1] is consistent with the expected topological band structure, but does not prove their chiral nature.

Cold atoms trapped in optical lattices and subjected to synthetic gauge fields [6, 7] are an ideal platform for realizing topological insulating phases. Making topology manifest in experiments, however, is a fundamental challenge. In this context, transport experiments are conceivable [8] but technically demanding. Existing proposals

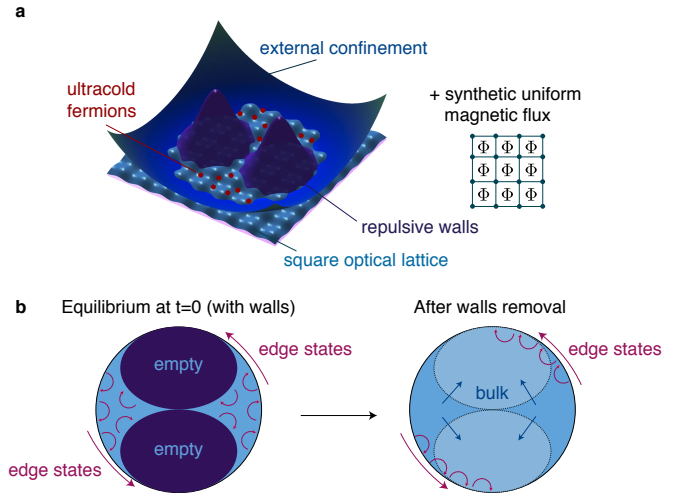


FIG. 1: Experimental scheme and general strategy. **a**, Trapped cold atomic fermions move on a square optical lattice in the presence of a synthetic uniform magnetic flux Φ . Two repulsive potentials, initially piercing holes in the atomic cloud, are suddenly removed at time $t = 0$. At all times, atoms are confined by an additional circular potential. We assume in this paper that the confining barriers are perfectly sharp, and discuss the case of smoother potentials in the Appendix E. **b**, The system is initially prepared in a quantum Hall phase: chiral edge states propagate along the edges determined by the repulsive walls and the external confinement. After releasing the walls, the edge states tend to propagate along the Fermi radius determined by the circular confinement: they encircle the initially vacant regions.

for measuring topological invariants [9–13] have experimental drawbacks and can only be applied to very specific configurations. Likewise, detecting topological edge

states [14–19], e.g., through light scattering methods [20], require complicated manipulations to separate the small edge-state signal from the bulk background [17].

Here, we introduce a simple method to directly visualize the propagation of topological edge modes, by studying the time evolution of an atomic QH system after suddenly releasing constraining walls, see Fig. 1. We show that the movement of the chiral edge states, encircling the initially vacant regions, is then directly visible in the atomic density. This allows us to evaluate the edge states angular velocity and to provide an unambiguous signature for the existence of chiral edge modes in the atomic system (Fig. 1). Our method is straightforward and insensitive to experimental imperfections: it only relies on a large initial occupancy of edge states. Crucially, our method requires that the edge states contribution to the density remains spatially separated from the bulk, which can be realized by populating a dispersionless bulk band with non-zero Chern number. We present several detection techniques, applicable to both flat and dispersive bands, that demonstrates the universal applicability to atomic systems with propagating edge modes.

We consider a two-dimensional optical lattice filled with non-interacting fermions, subjected to a uniform synthetic magnetic flux Φ [21, 22], and confined by a circular potential, $V_{\text{conf}}(r) = V_0(r/r_0)^\gamma$. In experiment, $V_{\text{conf}}(r)$ can be made nearly arbitrarily sharp ($\gamma \rightarrow \infty$) [23, 24]; this configuration is of particular interest for our scheme, as demonstrated in the Appendix E. The resulting system realizes the Hofstadter model [25] with second-quantized Hamiltonian

$$\hat{H} = -J \sum_{m,n} \hat{c}_{m+1,n}^\dagger \hat{c}_{m,n} + e^{i2\pi\Phi m} \hat{c}_{m,n+1}^\dagger \hat{c}_{m,n} + \text{h.c.} + \sum_{m,n} V_{\text{conf}}(r) \hat{c}_{m,n}^\dagger \hat{c}_{m,n}. \quad (1)$$

$\hat{c}_{m,n}^\dagger$ describes the creation of a fermion at lattice site $\mathbf{x}/a = (m, n) \in \mathbb{Z}^2$; J is the tunneling amplitude; and we take the lattice period a as our unit of length. This model has a topological band structure [1, 2]: When $\Phi = p/q \in \mathbb{Q}$, the bulk energy spectrum splits into q subbands [25], each associated with a non-zero Chern number [2]. This guarantees the existence of robust edge states in the bulk energy gaps [3]. These edge states are *chiral* in the sense that they propagate along the Fermi radius R_F (i.e., the edge of the atomic cloud delimited by the confining potential V_{conf}) with a definite orientation of propagation. It is convenient to represent such non-trivial spectra by diagonalizing the Hamiltonian (1) on a cylindrical geometry [3], see Fig. 2. This picture shows a clear separation of the bulk and edge states dispersions that survives in the experimental circular geometry produced by V_{conf} (Appendix E and Refs. [17, 26]). In the following, we specifically study the configurations $\Phi = 1/3$ and $\Phi = 1/5$ and set the Fermi energy $E_F = -1.5J$ inside the lowest bulk energy gap, see Fig. 2. In both these situations, the lowest energy band is

associated with the Chern number $\nu = -1$, which guarantees the occupancy of a single edge mode with same chirality $\text{sign}(\nu) = (-)$. These two configurations differ significantly in that the occupied bulk band is *nearly flat* (dispersionless) in the case $\Phi = 1/5$, while it is dispersive for $\Phi = 1/3$, see Fig. 2.

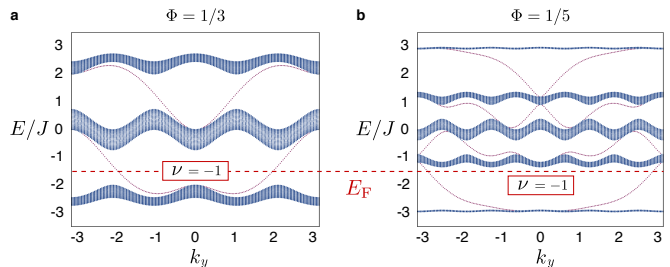


FIG. 2: **Bulk and edge states spectrum: dispersive vs flat bands.** Energy spectrum $E(k_y)$ as a function of the quasi-momentum k_y for **a**, $\Phi = 1/3$ and **b**, $\Phi = 1/5$, obtained by diagonalizing the Hamiltonian (1) on a finite cylinder directed along the x direction, with $V_{\text{conf}} = 0$. The projected bulk bands $E(k_x, k_y) \rightarrow E(k_y)$, shown in blue, are separated by large gaps of order $\sim J$. The red dispersion branches that are visible within the bulk gaps correspond to propagating modes that are localized on the opposite edges of the cylinder. When the Fermi energy is set within the first bulk gap, a single edge mode is populated on each edge of the cylinder (the lowest bulk band corresponds to the Chern number $\nu = -1$ for $\Phi = 1/q$). When considering the circular geometry realized in an experiment ($V_{\text{conf}} \neq 0$) and setting $E_F = -1.5J$, one is guaranteed that a single edge mode will be populated since the Chern number ν does not rely on the specific geometry used [17, 26]. Note that in the case $\Phi = 1/5$, the lowest energy band is characterized by the tiny flatness ratio, $f = W/\Delta \approx 0.04$, where $W(\Delta)$ denotes the first band (gap) width; in this topological quasi-flat band configuration, the populated edge states are expected to propagate more rapidly than the bulk.

Our scheme **(a)** demonstrates the existence of propagating modes that are localized close to the Fermi radius, and **(b)** identifies their angular velocity θ . To achieve this goal, we consider a geometry which constrains the QH system within two regions of the trap, as sketched in Figure 1, resembling a bat in flight. This initial “bat” geometry is shaped by a pair of sharp potential walls $V_{\text{hole}} = V_{\text{hole}1} + V_{\text{hole}2}$ defined by $(x \pm r_0/2)^2 + (y/\sqrt{2})^2 < r_0^2/4$, creating holes in the density distribution (see also Appendix F). In the bat geometry, we set the Fermi energy within the lowest bulk gap $E_F = -1.5J$ and suddenly remove V_{hole} at time $t = 0$. We then study the dynamics of the atomic density with all other parameters unchanged. The bat shape is optimized for visualizing the time-evolving chiral edge states in the density $\rho(\mathbf{x}, t)$ for $t > 0$, see Fig. 1b. In the following, we discuss how this “wall-removal” strategy can be exploited to reveal the edge states properties, as they progressively encircle the initially empty regions in a chiral manner.

Figure 3a shows the time-evolving density distribution $\rho(\mathbf{x}, t)$ for $\Phi = 1/3$. This example highlights the im-

portance of the bulk band structure, as it demonstrates the drawbacks encountered when preparing a system with *dispersive* bulk bands, see Fig. 2a. The time evolution in Fig. 3a, illustrates two main effects: (1) the progressive encircling of the holes by particles at the system's radial-edge (with localization length $\sim a$), and (2) the rapid filling of the holes by bulk states, see also Fig. 1b. Once $t \approx 10 - 20\hbar/J$, the atomic cloud's initial bat shape has become cyclonic, directly demonstrating the edge states' chirality. To provide further insight, we separately calculated the contribution stemming from the initially populated edge states, $\rho_{\text{edge}}(\mathbf{x}, t)$, see Appendix A. In the corresponding Fig. 3b, we observe that the edge states, which propagated along the edges delimited by the bat potential at $t < 0$, become localized along the circular edge at $r = R_F$, and that they follow a "chiral" motion. These edge states remain localized on the edge for very long times, and only slightly disperse into the bulk of the system, as can be anticipated from the small wavefunction overlap between edge and bulk states. Figure 3a emphasizes the problematic (non-chiral) filling of the holes by the many dispersive bulk states. The speed at which this filling occurs is to be compared with the circular motion of the edge states, which can be estimated from the group velocities $v = (1/\hbar)\partial E/\partial k$ associated with the bulk and edge states, see Fig. 2a. Additional interference takes place within the system, leading to small but visible patterns in the density. Figure 3b, shows that these patterns mainly originate from interferences between bulk states.

For $\Phi = 1/5$ and $E_F = -1.5J$, the dispersionless (flat) bulk band represented in Fig. 2b is totally filled, and most of the edge states lying in the first bulk gap are populated. The corresponding time-evolving density $\rho(\mathbf{x}, t)$, depicted in Fig. 4a, is radically different than for $\Phi = 1/3$, cf. Fig. 3a. For $\Phi = 1/5$, the edge states encircle the initially forbidden regions, largely unperturbed by the now motionless bulk. The dispersionless nature of the bulk states is further illustrated in Fig. 4c, which shows the evolution of $\rho_{\text{bulk}}(\mathbf{x}, t) = \rho(\mathbf{x}, t) - \rho_{\text{edge}}(\mathbf{x}, t)$. The initial bulk states are immobile for times $\sim 30\hbar/J$. In Fig. 4b, the evolution of the initially populated edge states $\rho_{\text{edge}}(\mathbf{x}, t)$ shows an interesting behavior: edge states with energies close to the flat bulk band are almost dispersionless, and remain localized on the edges delimited by the bat potential. Besides, the many dispersive edge states at higher energies encircle the holes in a clear and chiral manner. The instructive dynamics of the density $\rho(\mathbf{x}, t)$, which is due to the clear separation of the edge and bulk states during the evolution, can also be understood by studying the population of the single-particle eigenstates (Appendix A). Moreover, our method is highly robust against perturbations in the density (or equivalently in the Fermi energy, $E_F \approx -1.5J + \delta$), as it only relies on the occupation of dispersionless bulk states and sufficiently many edge states. We verified that the edge state signal is unambiguous when a high energy (dispersive) band is initially filled (Appendix D). We also found that this signal is immune to an additional random potential

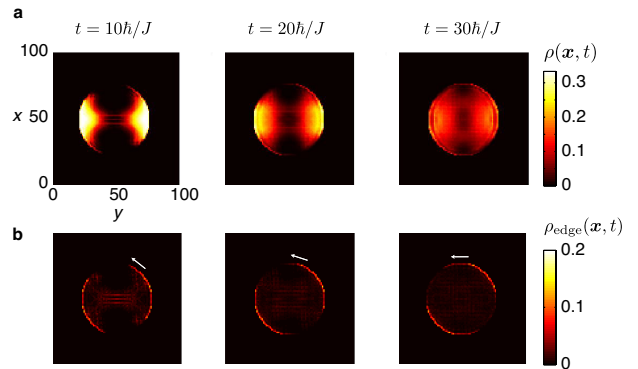


FIG. 3: **Evolution of the spatial densities after releasing the walls.** **a**, the spatial density $\rho(\mathbf{x}, t)$, and **b**, the contribution of the initially populated edge states $\rho_{\text{edge}}(\mathbf{x}, t)$. In all the figures, $\Phi = 1/3$, $E_F = -1.5J$ and we considered infinitely sharp circular confinement ($r_0 = 27a$) and ellipsoidal walls V_{hole} . The total number of particles is $N_{\text{part}} = 210$, while the number of initially populated edge states is $N_{\text{edge}} \approx 80$.

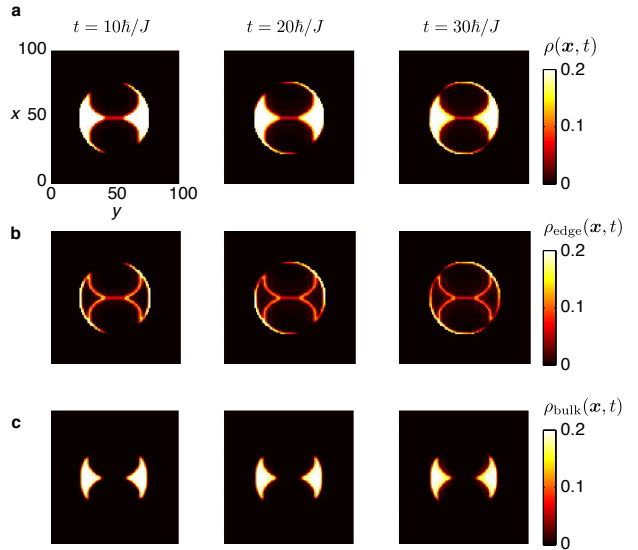


FIG. 4: **The topological quasi-flat band configuration.** **a**, the spatial density $\rho(\mathbf{x}, t)$, **b**, the contribution of the initially populated edge states $\rho_{\text{edge}}(\mathbf{x}, t)$, and **c**, the contribution of the initially populated bulk states $\rho_{\text{bulk}}(\mathbf{x}, t)$. In all the figures, $\Phi = 1/5$ and $E_F = -1.5J$. The total number of particles is $N_{\text{part}} = 146$, while the number of initially populated edge states is $N_{\text{edge}} \approx 64$. Note the *dispersionless* nature of the occupied bulk states, which highly improves the detection of the edge state signal.

$|V_{\text{rand}}(\mathbf{x})| \lesssim J$ mimicking disorder, in agreement with the chiral nature of the propagating states (Appendix G). Thanks to the topological quasi-flat band configuration, the edge states propagation can be visualized on long time scales, without being affected by the bulk dispersion. For $\Phi = 1/5$ and a typical system size $R_F \sim 100a$, we find $\dot{\theta} \sim 0.01J/\hbar$, which would require a realistic time $t \sim 70\hbar/J$ to observe the $\pi/4$ -rotation undergone by the edge states.

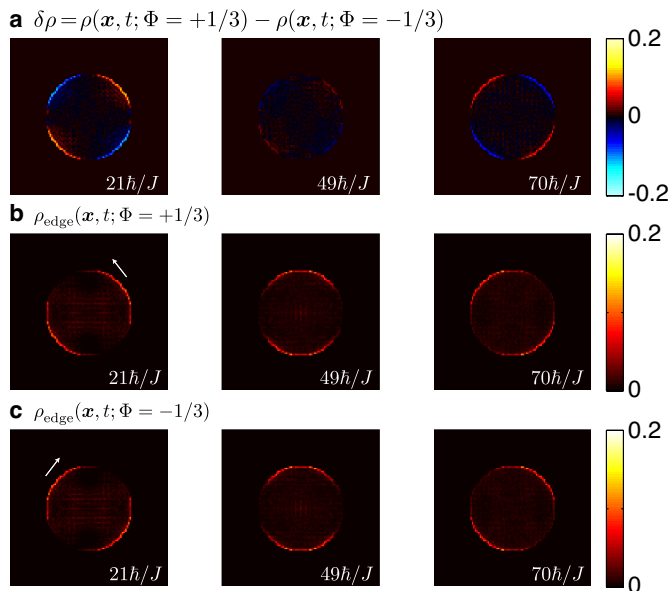


FIG. 5: **The opposite-flux method for dispersive systems.** **a**, Evolution of the difference $\delta\rho = \rho(\mathbf{x}, t; \Phi = +1/3) - \rho(\mathbf{x}, t; \Phi = -1/3)$, for the same configuration as in Figure 3. This method yields a clear manifestation of the edge states, $\delta\rho \approx \rho_{\text{edge}}(+\Phi) - \rho_{\text{edge}}(-\Phi)$, by eliminating the undesired contribution of the many bulk states. **b**, The edge-states contribution $\rho_{\text{edge}}(\mathbf{x}, t)$ for $\Phi = +1/3$, and **c**, for $\Phi = -1/3$. In the central column, we note the vanishing of the signal $\delta\rho(\mathbf{x}) \approx 0$ that occurs at time $t^* \sim 49\hbar/J$, indicating that the edge states angular velocity is $\dot{\theta} \sim 0.03J/\hbar$ for $R_F = 27a$ and $\gamma = \infty$ (also see Appendix B).

We now describe two methods for isolating the edge-states contribution ρ_{edge} from that of the bulk states, useful for systems with dispersive bulk bands. The first method consists in performing two successive experiments, using the same apparatus and parameters, but with opposite fluxes Φ and $-\Phi$. The difference between the two images $\delta\rho(\mathbf{x}, t) = \rho(\mathbf{x}, t; +\Phi) - \rho(\mathbf{x}, t; -\Phi)$, lacks the non-chiral contribution of the bulk states and is simply given by $\delta\rho \approx \rho_{\text{edge}}(+\Phi) - \rho_{\text{edge}}(-\Phi)$, see Fig. 5. For our bat geometry, $\rho_{\text{edge}}(+\Phi) \approx \rho_{\text{edge}}(-\Phi)$ when the edge states have undergone a rotation of $\theta = \pi/2$. This determines the time $t^* = \pi/(2\dot{\theta})$ when the signal $\delta\rho(\mathbf{x}, t^*)$ disappears, giving the angular velocity of the edge states (Appendix B). This situation is illustrated in Fig. 5 for the $\Phi = 1/3$ “dispersive” case, where we find $\delta\rho(\mathbf{x}, t^* \sim 49\hbar/J) \approx 0$, in good agreement with the angular velocity $\dot{\theta}_e \approx 0.03J/\hbar$ of the populated edge states [17]. We verified that slight differences in the filling [e.g., $E_F(\Phi_+ = +1/3) \sim E_F(\Phi_- = -1/3) \pm 0.1J$], for example

due to finite temperature effects between the two successive experiments, or variations in the flux (e.g., $\Phi_+ = 1/3$ and $\Phi_- \approx -\Phi_+ \pm 0.01$), do not significantly affect the signal $\delta\rho(\mathbf{x}, t)$, highlighting the robustness of this method against experimental imperfections.

The second method aims to efficiently reduce the bulk dispersion by suddenly *lowering* the potential walls V_{hole} at $t = 0$, instead of removing them completely. This operation can be achieved in such a way that only the edge states with sufficiently high energies are allowed to propagate, while leaving the bulk states away from the holes. This “edge-filter method” can be realized by setting the Fermi energy within the first bulk gap, and then suddenly lowering the potential V_{hole} to the value $V_{\text{hole}}^{t>0} \sim W$ at $t = 0$, where W is the width of the lowest bulk band. The great efficiency of this method is presented in the Appendix C for the case $\Phi = 1/3$.

Our results are stable when the spacious ellipsoidal walls are replaced by small perturbative potentials (Appendix F). Moreover, using a gaussian potential instead of the infinitely sharp potential V_{hole} gives equivalent results (Appendix E). In contrast, a sharp external confinement $V_{\text{conf}}(r) \sim r^\gamma$ with $\gamma \sim \infty$, is desirable for detecting the edge states motion in reasonable times, since the edge-state velocity dramatically decreases as the potential is smoothed [17]. Furthermore, the radii R_e at which the edge states ϕ_e localize are energy-dependent $R_e \sim \sqrt[\gamma]{\epsilon_e}$, leading to a spatial broadening of the edge state signal for finite γ (Appendix E). The schemes introduced in this work to reduce, or even eliminate, the irrelevant contribution of dispersive bulk states can be applied to a wide family of topological atomic systems, such as the promising Haldane-like optical lattice [9, 11] and fractional QH atomic gases [27, 28]. Finally, our method can be directly extended to visualize the propagation of Z_2 topological (spin-polarized) edge states, both in 2D [15, 29] and 3D [30], by using standard spin-dependent imaging methods.

We acknowledge discussions with J. Beugnon, I. Bloch, G. Bulnes Cuetara, M. Müller and S. Nascimbène. This work was supported by the FRS-FNRS (Belgium), ANR AGAFON, ERC QUAGATUA. Work at Innsbruck is supported by the integrated project AQUITE, the Austrian Science Fund through SFB F40 FOQUS, and by the DARPA OLE program. IBS acknowledges the financial support of the NSF through the Physics Frontier Center at JQI, and the ARO with funds from both the Atomtronics MURI and DARPA OLE Program.

[1] M. Z. Hasan and C. L. Kane, *Rev. Mod. Phys.* **82**, 3045 (2010).
[2] M. Kohmoto, *Phys. Rev. B* **39**, 11943 (1989).
[3] Y. Hatsugai, *Phys. Rev. Lett.* **71**, 3697 (1993).
[4] R. C. Ashoori, H. L. Stormer, L. N. Pfeiffer, K. W. Baldwin and K. West, *Phys. Rev. B* **45**, 3894 (1992).

[5] Y. Zhang *et al.*, *Phys. Rev. B* **79**, 241304 (2009).
[6] M. Aidelsburger *et al.*, *Phys. Rev. Lett.* **107**, 255301 (2011).
[7] J. Dalibard, F. Gerbier, G. Juzeliūnas and P. Öhberg, *Rev. Mod. Phys.* **83**, 1523 (2011).

- [8] J.P. Brantut, J. Meineke, D. Stadler, S. Krinner and T. Esslinger, *Science* **337**, 1069 (2012).
- [9] E. Alba, X. Fernandez-Gonzalvo, J. Mur-Petit, J. K. Pachos and J. J. Garcia-Ripoll, *Phys. Rev. Lett.* **107**, 235301 (2011).
- [10] E. Zhao, N. Bray-Ali, C. Williams, I. B. Spielman and I. Satija, *Phys. Rev. A* **84**, 063629 (2011).
- [11] N. Goldman *et al.*, arXiv:1209.1126 (2012).
- [12] H. M. Price and N. R. Cooper, *Phys. Rev. A* **85**, 033620 (2012).
- [13] R. O. Umucalilar, H. Zhai, and M. Ö. Oktel, *Phys. Rev. Lett.* **100**, 070402 (2008).
- [14] V. W. Scarola and S. Das Sarma, *Phys. Rev. Lett.* **98**, 210403 (2007).
- [15] N. Goldman *et al.*, *Phys. Rev. Lett.* **105**, 255302 (2010).
- [16] T. D. Stanescu, V. Galitski and S. Das Sarma, *Phys. Rev. A* **82**, 013608 (2010).
- [17] N. Goldman, J. Beugnon and F. Gerbier, *Phys. Rev. Lett.* **108**, 255303 (2012).
- [18] M. Killi and A. Paramekanti, *Phys. Rev. A* **85**, 061606(R) (2012).
- [19] C. V. Kraus, S. Diehl, P. Zoller and M. A. Baranov, *New J. Phys.* **14**, 113036 (2012).
- [20] S. B. Papp *et al.*, *Phys. Rev. Lett.* **101**, 135301 (2008).
- [21] D. Jaksch and P. Zoller, *New J. Phys.* **5**, 56 (2003).
- [22] F. Gerbier and J. Dalibard, *New J. Phys.* **12**, 033007 (2010).
- [23] T. P. Meyrath, F. Schreck, J. L. Hanssen, C.-S. Chuu and M. G. Raizen, *Phys. Rev. A* **71**, 041604(R) (2005).
- [24] A. L. Gaunt, T. F. Schmidutz, I. Gotlibovych, R. P. Smith and Z. Hadzibabic, arXiv:1212.4453 (2012).
- [25] D. R. Hofstadter, *Phys. Rev. B* **14**, 2239 (1976).
- [26] M. Buchhold, D. Cocks and W. Hofstetter, *Phys. Rev. A* **85**, 63614 (2012).
- [27] N. R. Cooper, *Adv. Phys.* **57**, 539 (2008).
- [28] A. S. Sørensen, E. Demler and M. D. Lukin, *Phys. Rev. Lett.* **94**, 086803 (2005).
- [29] B. Béri and N. R. Cooper, *Phys. Rev. Lett.* **107**, 145301 (2011).
- [30] A. Bermudez *et al.*, *Phys. Rev. Lett.* **105**, 190404 (2010).

Appendix A: The time evolution and observable quantities

The system is prepared in the ground-state of the initial Hamiltonian,

$$\hat{H}_0 = \hat{H} + \sum_{m,n} V_{\text{hole}}(m,n) \hat{c}_{m,n}^\dagger \hat{c}_{m,n}, \quad (\text{A1})$$

where the potential V_{hole} describes the walls initially present in the trap (see main text), and where \hat{H} is given by Eq. (1). We denote the number of available sites before and after removing the walls by n_{sites}^0 and n_{sites} , respectively, and we define the ratio $(1 - \eta) = n_{\text{sites}}^0/n_{\text{sites}}$. When $V_{\text{hole}} = 0$, the total number of sites within the trap is approximatively given by the area $n_{\text{site}} \approx \pi(r_0/a)^2$, while the outer circular edge contains about $n_{\text{edge}} \approx 2\pi r_0/a$ lattice sites. The holes in the density created by V_{hole} correspond to $n_{\text{hole}} = n_{\text{sites}} - n_{\text{sites}}^0 \approx \pi(r_0/a)^2/\sqrt{2}$ vacant sites, leading to the large ratio $\eta = n_{\text{hole}}/n_{\text{sites}} \approx 1/\sqrt{2}$. For $r_0 = 27a$, the system initially contains $n_{\text{site}}^0 \approx 700$

sites and the number of sites delimiting the edge of the bat is $n_{\text{edge}}^0 \approx 320$ sites. Thus, the spacious holes used in our calculations lead to a large edge/bulk ratio. For $\Phi \approx p/q \in \mathbb{Q}$, and initially setting the Fermi energy in the lowest bulk gap, leads to the filling factor $\nu^0 = N_{\text{part}}/n_{\text{sites}}^0 \sim 1/q$. After removing the walls V_{hole} , the filling factor is reduced to the smaller value $\nu = N_{\text{part}}/n_{\text{sites}} \sim (1 - \eta)/q \ll \nu^0$.

The groundstate of Hamiltonian (A1) is written as

$$|\Psi_0\rangle = \prod_{E_\alpha < E_F} \hat{f}_\alpha^\dagger |\emptyset\rangle, \quad (\text{A2})$$

where the operator \hat{f}_α^\dagger creates a particle in the single-particle state $|\chi_\alpha\rangle$, with energy E_α located below the Fermi energy E_F . Here $\{|\chi_\alpha\rangle, E_\alpha\}$ represents the complete set of single-particle eigenstates and eigenvalues satisfying the stationary Schrödinger equation

$$\hat{H}_0 |\chi_\alpha\rangle = E_\alpha |\chi_\alpha\rangle. \quad (\text{A3})$$

We are interested in the time evolution of the spatial density $\rho(\mathbf{x}, t)$ after removing the walls V_{hole} at $t = 0$. The evolution of the single-particle states $|\chi_\alpha\rangle$ is then entirely governed by the Hamiltonian \hat{H} . It is therefore convenient to introduce the eigenstates and eigenvalues $\{|\phi_\lambda\rangle, \epsilon_\lambda\}$ corresponding to the Hamiltonian \hat{H} ,

$$\hat{H} |\phi_\lambda\rangle = \epsilon_\lambda |\phi_\lambda\rangle. \quad (\text{A4})$$

We then introduce the notation $|\chi_\alpha(t)\rangle$, which corresponds to the time evolution of the initial state $|\chi_\alpha\rangle$ according to the Hamiltonian \hat{H} ,

$$|\chi_\alpha(t)\rangle = \sum_\lambda \langle \phi_\lambda | \chi_\alpha \rangle e^{-i\epsilon_\lambda t/\hbar} |\phi_\lambda\rangle. \quad (\text{A5})$$

The spatial density $\rho(\mathbf{x}, t)$ at time t is given by

$$\begin{aligned} \rho(\mathbf{x}, t) &= \langle \Psi(t) | \hat{c}_{m,n}^\dagger \hat{c}_{m,n} | \Psi(t) \rangle \\ &= \langle \Psi_0 | \hat{c}_{m,n}^\dagger(t) \hat{c}_{m,n}(t) | \Psi_0 \rangle, \end{aligned} \quad (\text{A6})$$

where $|\Psi_0\rangle$ is the initial ground state in Eq. (A2). Here, we introduced the Heisenberg representation of the field operators

$$\begin{aligned} \hat{c}_{m,n}^{(\dagger)}(t) &= e^{i\hat{H}t/\hbar} \hat{c}_{m,n}^{(\dagger)} e^{-i\hat{H}t/\hbar} \\ &= \sum_\alpha \chi_\alpha^{(*)}(\mathbf{x}, t) \hat{f}_\alpha^{(\dagger)}, \end{aligned} \quad (\text{A7})$$

where $\chi_\alpha(\mathbf{x}, t) = \langle \mathbf{x} | \chi_\alpha(t) \rangle$ is given by Eq. (A5). From Eqs. (A2),(A6),(A7), one finds the simple result

$$\rho(\mathbf{x}, t) = \sum_{E_\alpha < E_F} |\chi_\alpha(\mathbf{x}, t)|^2, \quad (\text{A8})$$

namely, that the particle density $\rho(\mathbf{x}, t)$ is entirely governed by the time-evolution of the initially occupied single-particle states. The time evolution of the atomic

cloud, after releasing the walls V_{hole} at $t = 0$, can therefore be numerically evaluated through a direct diagonalization of the Hamiltonians \hat{H} and \hat{H}_0 . In our study, a crucial aspect consists in identifying the regimes for which the edge states propagating around the initially forbidden regions provide a clear signal, which is not perturbed by the many bulk states. It is therefore desirable to separately evaluate the contributions of the initially populated bulk and edge states. We introduce the corresponding quantities

$$\begin{aligned}\rho_{\text{edge}}(\mathbf{x}, t) &= \sum_{E_e < E_F} |\chi_e(\mathbf{x}, t)|^2, \\ \rho_{\text{bulk}}(\mathbf{x}, t) &= \rho(\mathbf{x}, t) - \rho_{\text{edge}}(\mathbf{x}, t),\end{aligned}$$

where the sum $\sum_{E_e < E_F}$ is restrained to the populated edge states with energies E_e located within the bulk gap.

In this study, the time evolution is chosen to be entirely dictated by the Hamiltonian \hat{H} , and thus, it is non-dissipative: after releasing the walls, the total energy of the system is constant and is given by

$$\mathcal{E}_0 = \langle \Psi_0 | \hat{H} | \Psi_0 \rangle \approx \sum_{E_\alpha < E_F} E_\alpha, \quad (\text{A9})$$

where we considered the approximation $\langle \Psi_0 | \hat{H} | \Psi_0 \rangle \approx \langle \Psi_0 | \hat{H}_0 | \Psi_0 \rangle$, which is valid for V_{hole} sufficiently abrupt. For example, in the situation illustrated in Fig. 4, the energy released after removing the walls is about $J/3$. Therefore, in our calculations, the many-body state $|\Psi(t)\rangle$ never reaches the ground state $|\Psi_{\text{GS}}\rangle$ of the final Hamiltonian \hat{H} , with energy

$$\mathcal{E}_{\text{GS}} = \langle \Psi_{\text{GS}} | \hat{H} | \Psi_{\text{GS}} \rangle. \quad (\text{A10})$$

This final ground state, which differs from the initially prepared ground state $|\Psi_0\rangle$ in Eq. (A2), is expressed as

$$|\Psi_{\text{GS}}\rangle = \prod_{\lambda=1}^{N_{\text{part}}} \hat{a}_\lambda^\dagger |\emptyset\rangle, \quad (\text{A11})$$

where \hat{a}_λ^\dagger creates a particle in the single-particle state $|\phi_\lambda\rangle$, with energy $\epsilon_\lambda < \epsilon_{\lambda+1}$. Here, $N_{\text{part}} = \sum_{E_\alpha < E_F}$ is the total number of particles in the system, which is supposed to be constant (see Figs. 6a-b). In our non-dissipative framework, the probability $\mathcal{P}_\lambda(t)$ of finding a particle in the eigenstate $|\phi_\lambda\rangle$ is constant and inferior to one, as it is simply given by

$$\begin{aligned}\mathcal{P}_\lambda(t) &= \langle \Psi(t) | \hat{a}_\lambda^\dagger \hat{a}_\lambda | \Psi(t) \rangle = \sum_{E_\alpha < E_F} |\langle \phi_\lambda | \chi_\alpha \rangle|^2 = \text{cst} < 1, \\ &\neq \langle \Psi_{\text{GS}} | \hat{a}_\lambda^\dagger \hat{a}_\lambda | \Psi_{\text{GS}} \rangle = 1 \text{ if } \lambda \leq N_{\text{part}} \text{ (otherwise 0)}. \quad (\text{A12})\end{aligned}$$

The populations \mathcal{P}_λ are illustrated as a histogram in Fig. 6c, for the case $\Phi = 1/5$ and $E_F = -1.5J$. We find that when the Fermi energy is initially set within the first bulk gap, the population of high-energy dispersive bulk bands is highly limited during the evolution, which guarantees a clear spatial separation of the bulk and edge signal in

this ‘‘topological quasi-flat band’’ configuration. The efficiency with which the initial edge modes χ_e project to the final edge modes ϕ_e is further shown in Fig. 7, indicating the success of our scheme. For the situation illustrated in Figs. 6-7, we find that the number of populated edge states $\mathcal{P}_{\text{edge}} = \sum_{\lambda \in \text{edge states}} \mathcal{P}_\lambda \approx 30 \approx N_{\text{edge}}/2$, where $N_{\text{edge}} \approx 64$ is the number of populated edge states before removing the walls (see main text). This result is in agreement with the fact that the edge delimited by the bat contains $n_{\text{edge}}^0 \approx 2 \times n_{\text{edge}}$ sites, where $n_{\text{edge}} \approx 2\pi r_0/a$ is the number of sites delimited by the external confinement.

In the main text, we discuss the non-dissipative evolution of the atomic cloud after releasing the walls V_{hole} , neglecting thermalization processes. However, it is instructive to estimate the energy loss that would be required to reach the ground state $|\Psi_{\text{GS}}\rangle$, namely $\delta\mathcal{E} = \mathcal{E}_0 - \mathcal{E}_{\text{GS}}$. We propose to evaluate this energy difference for a configuration which is particularly relevant for our work (see main text), namely, a system exhibiting large initial holes and a flat (dispersionless) lowest bulk band. In the following, we set the energy of the lowest bulk band equal to zero. The energy difference $\delta\mathcal{E}$ will generally be large in this ‘‘large hole/flat band’’ situation, since many bulk states become available in the lowest energy band after removing the walls, namely $\mathcal{E}_{\text{GS}} \sim 0$ [see Figs. 6a-b and below]. For this configuration, which is particularly suitable for visualizing the edge states encircling the holes, the energy difference is thus approximatively given by

$$\delta\mathcal{E} \approx \sum_{\text{occupied edge states } e} E_e, \quad (\text{A13})$$

where we considered the Fermi energy to be located inside the first bulk gap [see Fig. 6a-b]. For large holes $\eta = n_{\text{hole}}/n_{\text{sites}} \gg 0$, the final filling factor $\nu \ll 1/q$ such that the lowest bulk band will only be partially occupied when reaching the ground state $|\Psi_{\text{GS}}\rangle$, and thus $\mathcal{E}_{\text{GS}} \sim 0$. From a rough geometric argument, we expect about $N_{\text{edge}} \sim \pi R_F (2 + \sqrt{\eta})/a(q-1)$ available edge states in the lowest bulk gap of the initial system. Approximating the edge state branch as being linear inside the whole gap Δ , we find

$$\delta\mathcal{E} \sim \frac{\Delta\pi}{q-1} (R_F/a)(1 + 0.5\sqrt{\eta}), \quad (\text{A14})$$

which corresponds to an energy difference $\delta\mathcal{E} \sim 1.5(R_F/a)J$ in the case $\Phi = 1/5$. In a typical experiment, $R_F \sim 100a$, which would require an important energy loss $\delta\mathcal{E} \sim 150J$ to reach the ground state $|\Psi_{\text{GS}}\rangle$. We verified that the estimated energy difference $\delta\mathcal{E}$ in Eq. (A14) is in good agreement with a direct numerical evaluation of Eq. (A13), for the system illustrated in Fig. 4 (i.e., $\Phi = 1/5$, $\eta \approx 1/\sqrt{2}$ and $E_F = -1.5J$).

Appendix B: The opposite-flux method for dispersive bulk bands

In this Section, we discuss how the difference $\delta\rho(\mathbf{x}, t) = \rho(\mathbf{x}, t; +\Phi) - \rho(\mathbf{x}, t; -\Phi)$, obtained from two successive

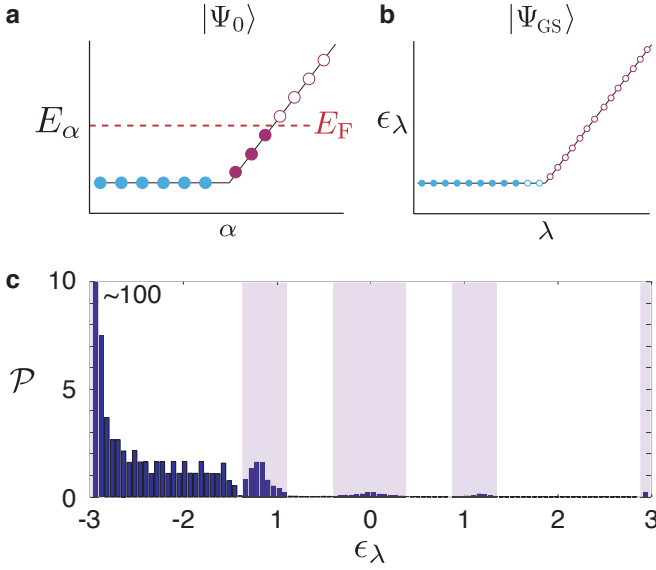


FIG. 6: **Ground states and single-particle states population.** Comparing **a**, the groundstate $|\Psi_0\rangle$ of the initially prepared system (with holes) and **b**, the groundstate $|\Psi_{GS}\rangle$ of the final system (without holes). Filled and empty blue (red) dots represent the occupied and unoccupied bulk (edge) states, respectively, with occupation number = 1. Note that the total number of particles, $N_{\text{part}} = \sum_{E_\alpha < E_F}$, is constant. **c** The population \mathcal{P} of the states $|\phi_\lambda\rangle$, as a function of their energy ϵ_λ , as established by the Fermi energy $E_F = -1.5J$ for the case illustrated in Fig. 4 (i.e., $\Phi = 1/5$, $\gamma = \infty$, $r_0 = 27a$ and $\eta \approx 0.7$). The energies corresponding to bulk states are emphasized by purple shaded regions, see Fig. 2b.

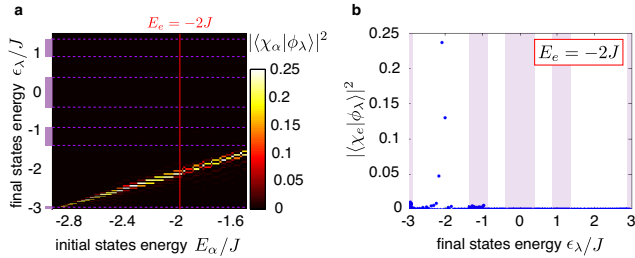


FIG. 7: **Wave-function overlaps between initial and final states.** **a**, The overlap $|\langle\chi_\alpha|\phi_\lambda\rangle|^2$ between the eigenstates of the initial (χ_α) and final (ϕ_λ) Hamiltonians, represented as a function of their energies. The parameters are the same as in Fig. 6. Note that the edge states are found in the bulk gap, namely, within the range $E \approx [-2.9J, -1.3J]$. **b**, Cut through the plot in Fig. **a**, for a specific initial edge state with energy $E_e = -2J$. The initial edge modes effectively project to the final edge modes, highly limiting the population of high energy (dispersive) bulk states. The energies corresponding to bulk states are emphasized by purple shaded regions in **a** and **b**.

measurements with opposite magnetic fluxes, is related to the edge states contributions $\rho_{\text{edge}}(\mathbf{x}, t; \pm\Phi)$. We show in Fig. 8a, the evolution of $\delta\rho(\mathbf{x}, t)$ for the dispersive case $\Phi = 1/3$, which clearly indicates that the contributions from the bulk $\rho_{\text{bulk}}(\mathbf{x}, t; +\Phi) \approx \rho_{\text{bulk}}(\mathbf{x}, t; -\Phi)$ vanish from the signal at all times $t = 7 - 70\hbar/J$. Accordingly, $\delta\rho(\mathbf{x}, t) \approx \rho_{\text{edge}}(\mathbf{x}, t; +\Phi) - \rho_{\text{edge}}(\mathbf{x}, t; -\Phi)$. To clarify the

evolution of this signal, which has non-vanishing values in the vicinity of the Fermi radius R_F , we show the chiral evolution of the edge states contribution $\rho_{\text{edge}}(\mathbf{x}, t; \pm\Phi)$ in Figs. 8b-c. At small times, the overlap between the two contributions $\rho_{\text{edge}}(\mathbf{x}, t; \pm\Phi)$ decreases in time, leading to a progressive broadening of the signal $\delta\rho(\mathbf{x}, t)$ along the 1D circular edge. Then, after reaching a rotation of $\theta \approx \pi/4$, the overlap increases, and eventually leads to a vanishing of the signal $\delta\rho(\mathbf{x}, t) \approx 0$ when the edge states have undergone a rotation of $\pi/2$, where $\rho_{\text{edge}}(\mathbf{x}, t; +\Phi) \approx \rho_{\text{edge}}(\mathbf{x}, t; -\Phi)$. In Fig. 8, this happens at time $t^* \sim 49\hbar/J$, indicating that the edge states angular velocity is $\dot{\theta} \sim 0.03J/\hbar$ for $R_F = 27a$. The opposite-flux method therefore offers a general technique for emphasizing the existence of chiral edge states in dispersive systems, and also, for evaluating their characteristic angular velocity.

We verified that a slight difference in the filling, $E_F(\Phi_+ = +1/3) \sim E_F(\Phi_- = -1/3) \pm 0.1J$, or variations in the flux, $\Phi_+ = 1/3$ and $\Phi_- \sim -\Phi_+ \pm 0.01$, does not significantly affect the signal $\delta\rho(\mathbf{x}, t)$ shown in Fig. 8a, highlighting the robustness of this method against possible experimental imperfections.

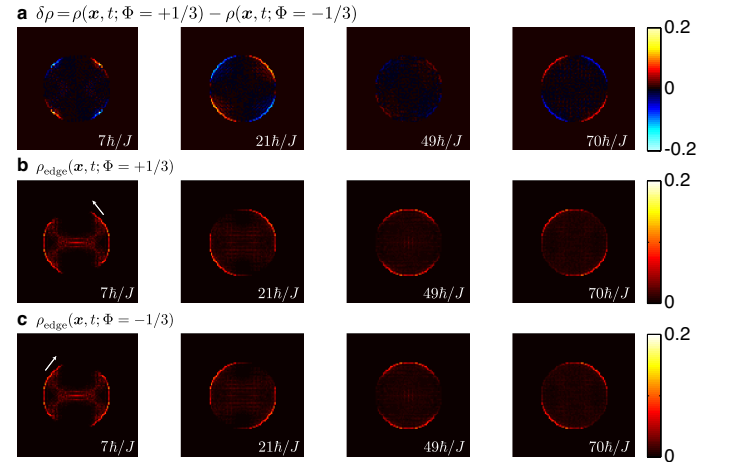


FIG. 8: **The opposite-flux method for dispersive systems.** **a**, Evolution of the difference $\delta\rho = \rho(\mathbf{x}, t; \Phi = +1/3) - \rho(\mathbf{x}, t; \Phi = -1/3)$, for the same configuration as in Figure 3. **b**, Evolution of the initially populated edge states $\rho_{\text{edge}}(\mathbf{x}, t)$ for $\Phi = +1/3$, and **c**, for $\Phi = -1/3$. The vanishing of the signal $\delta\rho(\mathbf{x}) \approx 0$ corresponds to a rotation of $\pi/2$. This happens at time $t^* \sim 49\hbar/J$, indicating that the edge state angular velocity is $\dot{\theta} \sim 0.03J/\hbar$ for $R_F = 27a$, in agreement with the results reported in Refs. [17].

Appendix C: The edge-filter method for dispersive bulk bands

Another strategy consists in allowing the edge states to propagate at $t > 0$, while *forbidding* the bulk states to penetrate the regions initially occupied by the holes. This can be achieved by suddenly lowering the additional potential walls V_{hole} to some intermediate value $V_{\text{hole}}^{t>0} \neq 0$, instead of removing them completely at $t = 0$. This

“edge-filter” scheme is illustrated in Fig. 9a, for the dispersive case $\Phi = 1/3$. By suddenly lowering the walls potential to the value $V_{\text{hole}}^{t>0} \approx W$, where W is the width of the lowest bulk band, we limit the undesired filling of the holes by the bulk states at times $t > 0$. In contrast, the populated edge states with energy $\epsilon_e > V_{\text{hole}}^{t>0} + \epsilon_{\text{min}}$, where ϵ_{min} is the minimum of the bulk band, are allowed to propagate around the holes without being spoiled by the bulk. The resulting time evolution of the density $\rho(\mathbf{x}, t)$, presented in Fig. 9b, shows a clear propagation of the edge states around the holes. Experimentally, this method offers an efficient method to isolate the edge states contribution from the spoiling bulk background, but it necessitates a very precise control over the potential strength V_{hole} .

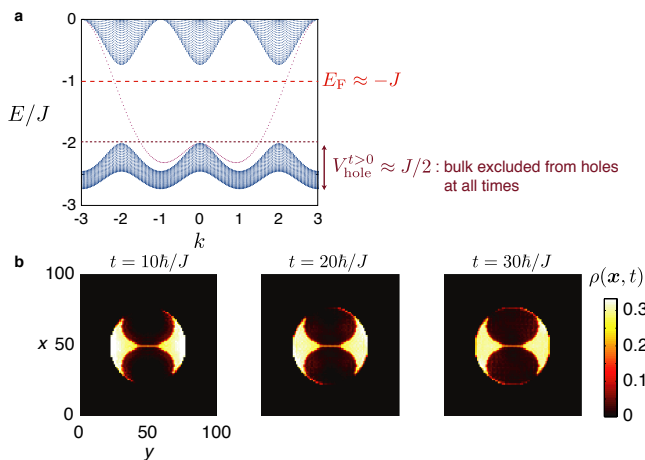


FIG. 9: **The edge-filter method for dispersive systems.** **a**, Energy spectrum $E(k)$ as a function of the quasi-momentum k for $\Phi = 1/3$. Also shown are the typical Fermi energy and the final walls potential strength $V_{\text{hole}}^{t>0} \approx W$, where W is the width of the lowest bulk band. **b**, Evolution of the spatial density $\rho(\mathbf{x}, t)$ for $\Phi = 1/3$, $E_F = -0.85J$, and infinitely abrupt confinement/walls. At $t = 0$, the strength of the hole potential is suddenly reduced to $V_{\text{hole}}^{t>0} = 0.5J$. Note that most of the bulk states are excluded from the holes during the evolution, yielding a clear edge-state signal, to be compared with Fig. 3 a.

Appendix D: Sensitivity to imperfect filling

Our general scheme is based on the possibility of preparing a QH atomic state, which can be achieved by generating a magnetic flux Φ in the lattice and filling the lowest bulk band completely. In other words, one has to tune the total number of particles N_{part} in such a way that the Fermi energy E_F lies within the lowest bulk gap. According to the topological nature of the lowest bulk band, one is then guaranteed that topological edge states are populated. In practice, the total number of particles (and the corresponding Fermi energy E_F) can be tuned with a great precision in cold-atom experiments. However, it is instructive to test the robustness of our method against inexact filling effects, in particular, for

the dispersionless case $\Phi = 1/5$. We remind that in this configuration, the clear separation of the bulk and edge states contributions to the density relies on the fact that the bulk states are dispersionless (they are described by a quasi-flat band). Here, we show that this picture holds even when the second (dispersive) bulk band is dramatically filled, see Fig. 10. From this result, we find that the high-energy bulk states contribute in a non-chiral manner to the density evolution, see Fig. 10, and that their dispersive motion is slow compared to the edge states propagation along the circular boundary. In particular, this shows that the chiral picture drawn by the density $\rho(\mathbf{x}, t)$, and which will be imaged in an experiment, can unambiguously be attributed to the populated edge states. We conclude that the edge-state signal obtained for the interesting case $\Phi = 1/5$ remains clear and detectable, as long as sufficiently many edge states are initially populated. In particular, this indicates that our scheme is robust at finite temperature $T > 0$, as long as it remains small compared to the gap’s width Δ , in order to insure a sufficiently large edge-state population.

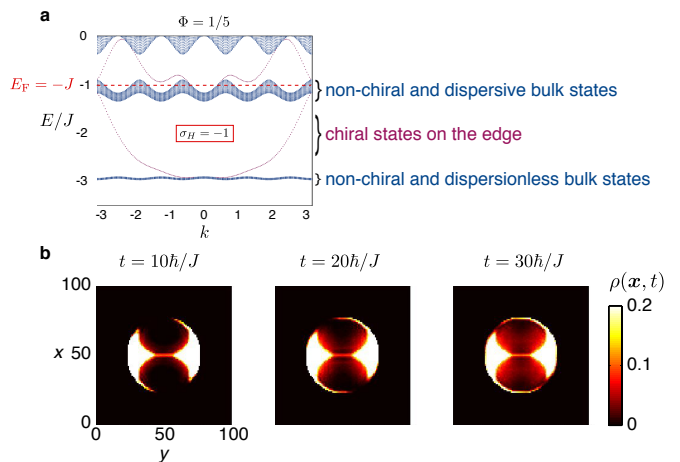


FIG. 10: **Sensitivity to imperfect filling in the flat-band configuration.** **a**, Energy spectrum $E(k)$ as a function of the quasi-momentum k for $\Phi = 1/5$, indicating the “dramatic” Fermi level $E_F = -J$ used in **b**, as well as the characteristics of the occupied states. **b**, Evolution of the spatial density $\rho(\mathbf{x}, t)$ for $E_F = -J$ and infinitely abrupt confinement/walls. Note the non-chiral behavior of the dispersive bulk states, to be compared with Fig. 4 a.

Appendix E: Gaussian walls and smooth circular confinements

When the magnetic flux $\Phi = 1/q$, with $q \in \mathbb{Z}$, the lowest bulk band is characterized by the Chern number $\nu = -1$. This result, which only relies on the topological order associated with the bulk, guarantees the existence of a single edge mode whose energy lies within the first bulk gap. This “topological robustness” of the edge states is maintained when using smooth confining potentials and when adding walls V_{hole} to the system, as long as these features do not destroy the bulk gaps. In

this Section, we show that the edge states lying within the first bulk gap survive for realistic confinements and gaussian walls. We then demonstrate that the density evolution $\rho(\mathbf{x}, t)$, previously shown for infinitely abrupt potentials (main text), are qualitatively equivalent for smooth potentials. We finally comment on the fact that it is highly desirable to design sharp confining potentials to improve the edge state signal in experiments.

In this Section, we focus on the case $\Phi = 1/5$, but we stress that the discussion holds for configurations that lead to similar band structures [16, 17, 26]). In the absence of walls $V_{\text{hole}} = 0$, the edge states lying in the first bulk gap are radially localized, with a radius determined by their energy and the circular confinement. Writing the circular confinement as $V_{\text{conf}}(r) = V_0(r/r_0)^\gamma$, we find that an edge state ϕ_e with energy ϵ_e is characterized by a localization radius

$$R_e = r_0 \sqrt[3]{|\epsilon_e - \epsilon_{\text{min}}|/V_0}, \quad (\text{E1})$$

where ϵ_{min} is the minimum of the bulk band. This result is illustrated in Fig. 11, for $r_0 = 21a$, $V_0 = J$ and $\gamma = \infty, 10, 4$, where the wavefunctions amplitudes $|\phi_\lambda(x, y)|^2$ are plotted as a function of the x coordinate, and their corresponding energies ϵ_λ . For an infinitely abrupt trap, $\gamma = \infty$, all the edge states are located at the constant Fermi radius $R_F = r_0$. Therefore, the edge states contribution to the density ρ_{edge} yields a clear circular signal, with localization length of the order of the lattice spacing a . In contrast, for finite γ , the populated edge states are localized on different radii $R_e \in [R_F - \delta r, R_F]$, leading to a broadening of the edge-state signal ρ_{edge} . For the situation illustrated in Fig. 11, this broadening is of the order $\delta r \sim 5a$ for $\gamma = 10$ and $\delta r \sim 10a$ for $\gamma = 4$. Let us stress another crucial aspect of these smoothly confined QH systems, which is the fact that the angular velocity $\dot{\theta}$ of the chiral edge states, as well as the number N_{edge} of available edge states within a bulk gap, highly depend on the potential's smoothness γ : the angular velocity is maximized for highly abrupt confinements ($\gamma \rightarrow \infty$), while the number N_{edge} is larger for smooth potentials [16, 17, 26]. We numerically evaluated the angular velocity of the edge states for $\Phi = 1/5$ and $r_0 = 21a$, and we found $\dot{\theta}_e \approx 0.06J/\hbar$ for $\gamma = \infty$, $\dot{\theta}_e \approx 0.02J/\hbar$ for $\gamma = 10$ and $\dot{\theta}_e < 0.01J/\hbar$ for $\gamma = 4$ (and we note that the angular velocity $\dot{\theta}_e \propto 1/R_e$). Scaling to a more realistic radius $r_0 = 100a$, we find that the edge states, which are populated below $E_F = -1.5J$, undergo a rotation of $\pi/5$ after a time

$$\begin{aligned} t(\theta = \pi/5) &\sim 50\hbar/J, & \gamma = \infty \ (r_0 = 100a), \\ t(\theta = \pi/5) &\sim 150\hbar/J, & \gamma = 10 \ (r_0 = 100a), \\ t(\theta = \pi/5) &\sim 300\hbar/J, & \gamma = 4 \ (r_0 = 100a), \end{aligned}$$

indicating that it is highly desirable to design a sharp circular confining trap $\gamma \gg 10$, to clearly observe the edge states rotating motion during reasonable experimental times $t \sim 10 - 100\hbar/J$.

We now investigate the density evolution $\rho(\mathbf{x}, t)$ for smooth confining traps and initial gaussian walls V_{hole} .

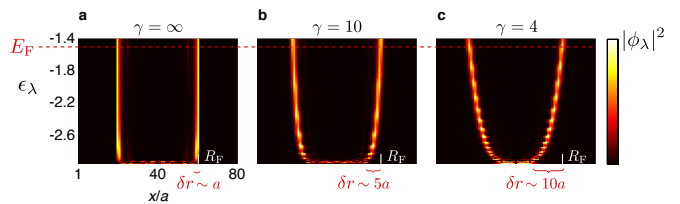


FIG. 11: **Smooth confinements and edge states.** The amplitudes $|\phi_\lambda(x, y)|^2$ of the single-particle wavefunctions as a function of the x coordinate and their corresponding energy ϵ_λ , and setting y at the center of the trap. Here, $\Phi = 1/5$, and the external potential is given by $V_{\text{conf}}(r) = V_0(r/r_0)^\gamma$, with $r_0 = 21a$ and $V_0 = J$. **a:** $\gamma = \infty$, **b:** $\gamma = 10$, and **c:** $\gamma = 4$. The Fermi radius R_F is shown for $E_F = -1.5J$. The populated edge states ϕ_e are localized on the radii $R_e = R_e(\epsilon_e)$, see Eq. (E1), leading to a broadening δr of their contribution to the spatial density ρ_{edge} for finite γ .

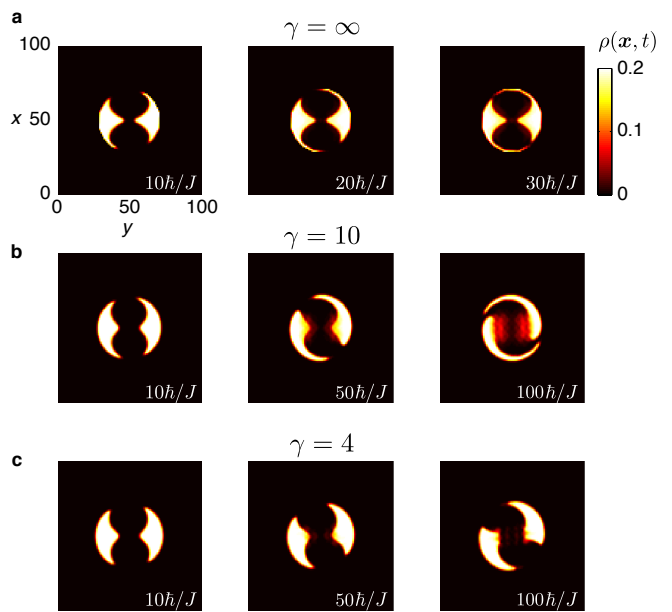


FIG. 12: **Smooth confinements and the density evolution.** Evolution of the spatial density for $\Phi = 1/5$ and $E_F = -1.5J$. The walls V_{hole} are produced by asymmetric gaussian potentials, with standard deviations $\sigma_y \approx \sqrt{2}\sigma_x$. The external confining potential is $V_{\text{conf}}(r) = V_0(r/r_0)^\gamma$, with $r_0 = 21a$ and $V_0 = J$. **a:** $\gamma = \infty$, **b:** $\gamma = 10$, and **c:** $\gamma = 4$. Note the broadening δr of the edge-state signal, see Fig. 11, and also, the deceleration of the motion as the confinement becomes smoother $\gamma = \infty \rightarrow 4$.

First of all, we note that the presence of gaussian walls does not destroy the edge states lying within the first bulk gap. In this bat geometry, the edge states are localized on the outer edge delimited by $V_{\text{conf}}(r)$, but also, on the smooth boundary delimited by the gaussian potentials. Therefore, when $\gamma \sim \infty$, the edge states behave as in Fig. 11a in the vicinity of the outer circular edge $r \approx r_0$, whereas they behave similarly as in Fig. 11c in the vicinity of the gaussian walls. We point out that, in our scheme, it is the behavior of the edge states near the outer circular edge which plays an important role. Indeed, as shown in Fig. 12a, replacing

the infinitely abrupt walls V_{hole} by gaussian potentials does not qualitatively affect the evolution of the density $\rho(\mathbf{x}, t)$ presented in Fig. 4a.

However, as can be anticipated from the discussion above, replacing the perfectly sharp potential $V_{\text{conf}}(r)$ by smoother confinements, $\gamma = \infty \rightarrow 4$, has dramatic consequences on the dynamics. In Fig. 12b, which shows the evolution of the density for $\gamma = 10$, we clearly observe the broadening $\delta r \sim 5a$ of the edge-state contribution $\rho_{\text{edge}}(\mathbf{x}, t)$, as they progressively encircle the holes. We also note the slower motion undergone by the edge states, which have a reduced angular velocity $\dot{\theta}(\gamma = 10) \sim \dot{\theta}(\gamma = \infty)/3$, see above. An even more dramatic situation is illustrated for the case $\gamma = 4$ in Fig. 12c. These results demonstrate the robustness of the edge state motion in the presence of smooth confining traps and gaussian walls, but they greatly emphasize the importance of designing sharp external confinements to improve the experimental detectability of the topological edge states.

Appendix F: The holes geometry and size effects

Our setup illustrated in Fig. 1 features two large repulsive potentials, which create the initial bat geometry. These holes are chosen to be created by infinitely abrupt walls V_{hole} , which are delimited by the two ellipses

$$(x \pm r_0/2)^2 + (y/\sqrt{2})^2 < r_0^2/4,$$

where the coordinates $(x, y) = 0$ at the center of the trap. This choice is motivated by the fact that these walls coincide (up to first order) with the external circular wall $V_{\text{conf}}(r)$ of radius r_0 , in the vicinity of the poles located at $(\pm r_0)\mathbf{1}_x$. Note that in the following of this discussion, we consider that $V_{\text{conf}}(r) \propto (r/r_0)^\gamma$ with $\gamma = \infty$.

The geometry produced by these potentials is particularly suitable to emphasize the edge states motion at time $t > 0$, as they encircle the regions initially surrounded by the elliptical walls. However, in this exotic geometry, the large holes correspond to a massive distortion of the standard circular system. It is thus interesting to study the validity of our method, as we progressively reduce the size of the holes. Here, we demonstrate that our scheme still shows a clear manifestation of the edge states, even in the limit where the walls V_{hole} only represent a small perturbation of the system, in the vicinity of its circular boundary. To analyze this, we propose to calculate the time evolution of the density $\rho(\mathbf{x}, t)$ after removing the elliptical walls delimited by the more general equations

$$(x \pm (b-1)r_0/b)^2 + (y/\sqrt{b})^2 < (r_0/b)^2, \quad (\text{F1})$$

which can be made arbitrarily small ($b \gg 1$), while maintaining the smooth contact with $V_{\text{conf}}(r)$ at the poles. The results are shown in Fig. 13 for the flat-band configuration previously studied in Fig. 4 (for $b = 2$), but with smaller initial holes $b = 4, 8, 16$. This picture emphasizes the fact that our scheme still allows to detect the chiral

motion of the edge states, in the limit of small perturbative walls V_{hole} . However, we stress that it is crucial to prohibit any broadening of the edge state signal in the perturbative regime $b \gg 2$, which necessarily requires the use of an extremely abrupt external potential V_{conf} with $\gamma \sim \infty$ (Appendix E). Moreover, considering smaller holes also demands to further reduce the bulk dispersion, which can be achieved by considering the quasi-flat-band configuration $\Phi = 1/5$, see Fig. 13, or by exploiting the “opposite-flux” or “edge-filter” methods.

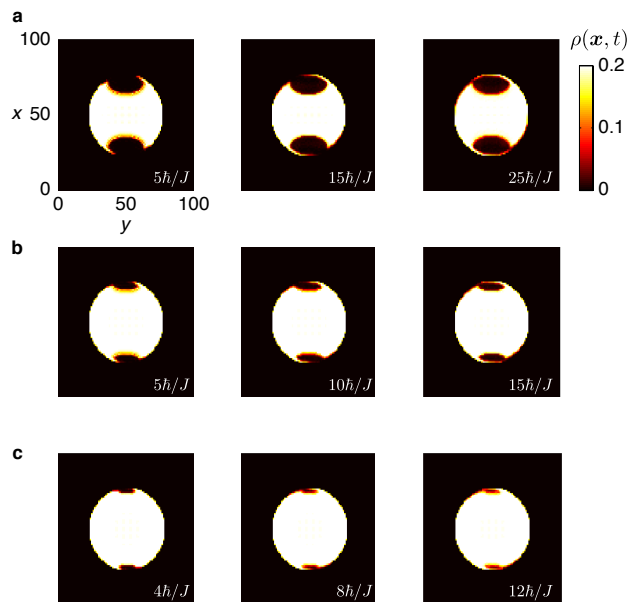


FIG. 13: **Effects of the holes size.** The spatial density $\rho(\mathbf{x}, t)$ for $\Phi = 1/5$, $E_F = -1.5J$, $r_0 = 27a$ and $\gamma = \infty$. The holes are described by Eq. (F1) and correspond to **a**, $b = 4$, **b**, $b = 8$, and **c**, $b = 16$. Note that the chiral motion of the edge states is still visible, even in the limit of tiny perturbative walls V_{hole} .

Appendix G: Robustness of the edge states against disorder

We finally investigate the robustness of the edge states motion in the presence of disorder. This perturbation, which plays a fundamental role in solid-state systems, can be engineered in optical-lattice setups, e.g., using speckle potentials. We study the effects of disorder by considering a random potential V_{rand} , with energies uniformly distributed within the range $V_{\text{rand}}(\mathbf{x}) \in [-D, D]$. The results are presented in Fig. 14, for the case $\Phi = 1/5$. We find that the chiral edge states signal remains robust for disorder strengths $D \lesssim 1.5J \approx \Delta$, where Δ is the size of the bulk gap. Interestingly, we can still distinguish a cyclonic cloud – a signature of the edge states chirality – for values up to $D \sim 3J \approx 2\Delta$. The immunity of the chiral edge states against disorder, a hallmark of the quantum Hall effect, could thus be demonstrated using our cold-atom setup.

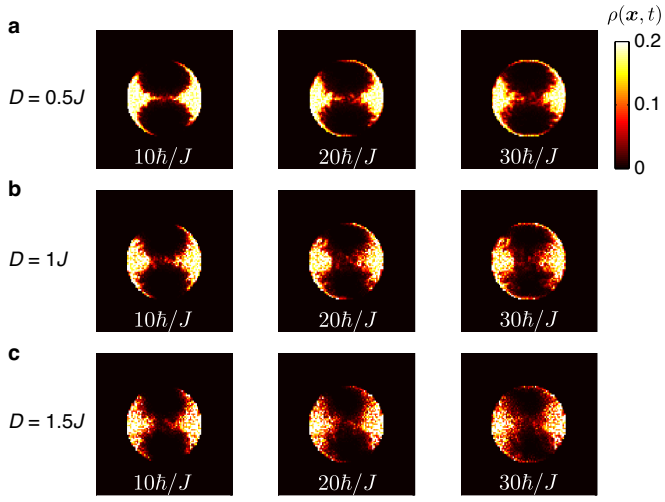


FIG. 14: **Effects of disorder.** The spatial density $\rho(\mathbf{x}, t)$ for $\Phi = 1/5$, $E_F = -1.5J$, $r_0 = 27a$ and $\gamma = \infty$. The disorder strength is **a**, $D = 0.5J$, **b**, $D = 1J$ and **c**, $D = 1.5J$.